Journal of Magnetism and Magnetic Materials 473 (2019) 241–252

Contents lists available at ScienceDirect

Journal of Magnetism and Magnetic Materials

journal homepage: www.elsevier.com/locate/jmmm

Research articles

Dual targeted magnetic photosensitive liposomes for photothermal/photodynamic tumor therapy

Anilkumar T.S.[a], Yu-Jen Lu[b], Huai-An Chen[a], Hao-Lung Hsu[a], Gils Jose[a], Jyh-Ping Chen[a,c,d,e,*]

[a] Department of Chemical and Materials Engineering, Chang Gung University, Kwei-San, Taoyuan 33302, Taiwan, ROC
[b] Department of Neurosurgery, Chang Gung Memorial Hospital, Linkou, Kwei-San, Taoyuan 33305, Taiwan, ROC
[c] Department of Plastic and Reconstructive Surgery and Craniofacial Research Center, Chang Gung Memorial Hospital, Kwei-San, Taoyuan 33305, Taiwan, ROC
[d] Research Center for Chinese Herbal Medicine and Research Center for Food and Cosmetic Safety, College of Human Ecology, Chang Gung University of Science and Technology, Kei-San, Taoyuan 33302, Taiwan, ROC
[e] Department of Materials Engineering, Ming Chi University of Technology, New Taipei City 24301, Taiwan, ROC

ARTICLE INFO

Keywords:
Magnetic liposomes
Magnetic nanoparticles
Indocyanine green
Photothermal therapy

ABSTRACT

In this work, we prepared a nano-vehicle for dual targeted (magnetic and ligand) and dual mode (photothermal/photodynamic) cancer therapy. For this purpose, magnetic photosensitive liposomes (MPLs) from 1,2-distearoyl-sn-glycero-3-phosphocholine, dimethyldioctadecyl ammonium bromide (DDAB) and cholesterol were prepared using solvent evaporation/hydration technique to encapsulate the photosensitizer indocyanine green (ICG) and citric acid-coated MNPs (CMNPs). Hyaluronic acid-polyethylene glycol (HA-PEG) was coated to the MPLs by self-assembly of HA-PEG on liposome surface through ionic interactions between negatively charged HA and positively charged lipid DDAB to fabricate HA-PEG-MPLs with ~220 nm particle size. The HA-PEG-MPLs aqueous solution showed highly efficient photothermal effects as the solution temperature reaches 45 °C in 3 min after exposure to near infrared (NIR) 808 nm laser at 2 W/cm^2. The in vitro cell culture experiments after treating human glioblastoma cells (U-87MG) with HA-PEG-MPLs confirmed enhanced cytotoxicity after 4 min exposure to NIR laser. A xenograft tumor model from subcutaneously implanted U87MG cells in nude mice demonstrated accumulation of HA-PEG-MPLs at tumor sites. By combination with successive NIR laser treatment, tumor growth could be prevented and the tumor volume at the end of treatment was 12.7% that of the control. Excellent and consistent anti-tumor efficacy with laser + HA-PEG-MPLs treatment was also demonstrated from the survival rates of animals, in vivo bioluminescence imaging and histology of tumor sections.

1. Introduction

As one of the biggest diseases in the world challenging the lives of all age groups, cancer is uncontrolled growth of cells, which may occur in any kind of tissue in the human body. Surgery, chemotherapy and radiation therapy are the main anti-tumor therapeutic approaches. Nonetheless, chemotherapy is associated with the downside effect of non-specific targeting of cancer cells and destroying normal/healthy cells apart from cancer cells during the course of the treatment [1]. To overcome this undesirable effect, targeted delivery of chemotherapeutic drugs with nano-carriers was introduced to transport drugs precisely to the tumor site for killing cancer cells [2,3]. Liposomes have been widely studied as effective nano-carriers for drugs because they are biocompatible and biodegradable and can be loaded with large quantities of drugs [4]. Liposomes surface could be also modified with ligand molecules that would be recognized by receptor molecules on the surface of cancer cells, such as antibodies, folic acid and hyaluronic acid (HA) to increase the intracellular cellular uptake of liposomes into tumor cells [5]. In addition, liposomes with a “stealth” property could be prepared by modification with polyethylene glycol (PEG) on liposome surface to prevent its rapid clearance by the mononuclear phagocyte system during circulation and increase liposome half-life in vivo [6]. In the past decade, liposomal formulations have been broadly used to enhance the effectiveness of drug delivery via several paths. The favourable outcome of liposomes as drug carriers have been echoed in a number of liposome-based formulations, which are commercially available or currently undergoing clinical trials [7–9].

Photothermal therapy (PTT) and photodynamic therapy (PDT) are alternative therapies to treat cancer. In PDT, a specific photosensitizer (PS) was irradiated with a specific wavelength of light, which leads to energy transfer to oxygen molecules by generating cytotoxic reactive oxygen species (ROS) [10]. The ROS can rapidly cause significant

* Corresponding author at: 259 Wen-Hwa 1st Road, Kwei-San, Taoyuan 33302, Taiwan, ROC.
E-mail address: jpchen@mail.cgu.edu.tw (J.-P. Chen).

https://doi.org/10.1016/j.jmmm.2018.10.020
Received 24 June 2018; Received in revised form 2 October 2018; Accepted 4 October 2018
Available online 09 October 2018
0304-8853/

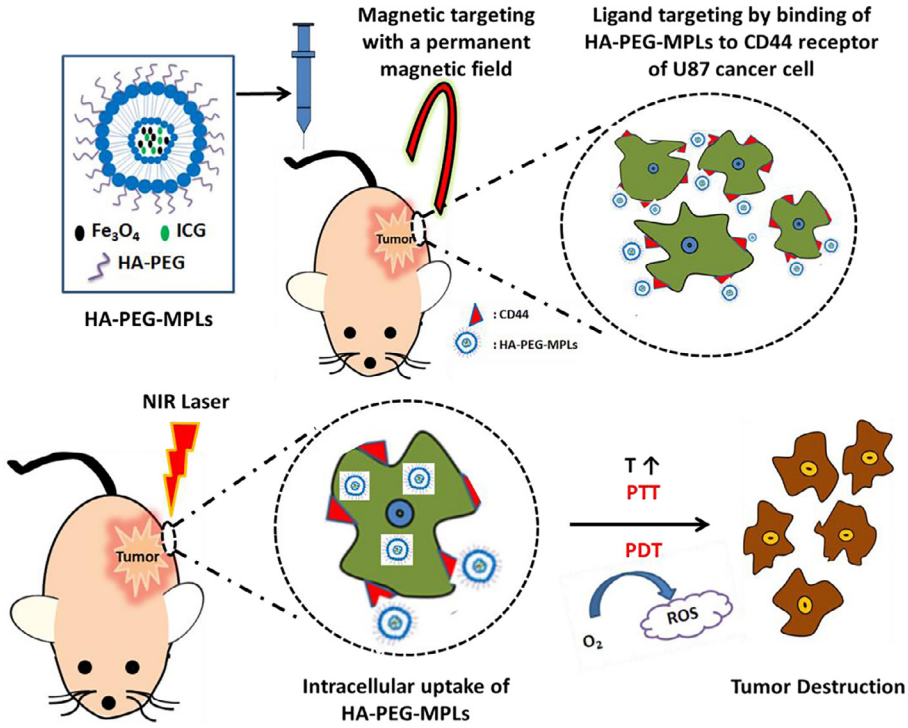

Fig. 1. Schematic illustration of HA-PEG-MPLs for dual targeted photothermal/photodynamic cancer therapy.

toxicity, leading to cell death via apoptosis or necrosis. On the other hand, the PS should be with minimally cytotoxicity in the absence of external photo-activating light. The PDT antitumor effects are driven based on three interrelated mechanisms, including direct cytotoxic effects on tumor cells, damage to the tumor vasculature and induction of a robust inflammatory reaction that can lead to development of systemic immunity [11,12]. Among several PS that acquire excitation energy in the near-infrared (NIR) region, ICG is the only approved clinical imaging and diagnosis agent by the U.S. Food and Drug Administration (FDA). ICG is also been widely applied to assess hepatic function, ophthalmic angiography, and surgical navigation [13,14]. The PTT is based on heat production when a photo-absorbing agent is irradiated with NIR laser light, as this heat can result in burning the cancer cells [14]. During the treatment, NIR laser light penetrates safely through the tissue to reach the tumor site. This penetrating NIR radiation can be transduced into local heat by a PTT agent accumulated in the cancer cells and thus cause effective damage of the targeted tumor regions. Different materials have been reported as a PTT agent, including organic compounds (e.g., ICG and polyaniline) inorganic nanomaterials (e.g., magnetic nanoparticles, metal chalcogenide, and carbon-based materials) [14–16].

Magnetic nanoparticles (MNPs) are effective guiding tool that could be driven to a precise targeted site with an external magnetic field. This advantageous factor of MNPs are widely exploited in many biomedical applications such as in targeted drug delivery systems and disease diagnosis [17]. By incorporating MNPs in liposomes, magnetic liposomes for site-specific accumulation of anticancer drugs in cancer cells by magnetic targeting were also reported [18]. Although the photothermal effect of MNPs after exposing to NIR laser is useful for PTT [19], supplementary of MNPs-based hyperthermia with other forms of cancer therapy such as chemotherapy, radiotherapy and combinatory PTT/PDT are deemed advantageous to enhance the therapeutic outcomes [20,21].

In this work, we developed dual targeted magnetic photosensitive liposomes (MPLs) for dual mode cancer therapy. Magnetic targeting was achieved by incorporating MNPs in liposomes while ligand targeting was accomplished by self-assembly of HA-PEG onto cationic MPLs to form HA-PEG-MPLs. In the latter approach, HA could bind with the over-expressed CD44 receptor on the cell surface of human primary glioblastoma cell line U87MG for receptor-mediated ligand targeting [22,23] while PEG helps to prolong the blood circulation of HA-liposomes in the body. With encapsulated ICG and MNPs within the aqueous core of liposomes, HA-PEG-MPLs were used as a PTT/PDT dual modal nano-sized therapeutic agent for efficient cancer therapy in vivo (Fig. 1).

2. Materials and methods

2.1. Materials

Fe (II) chloride tetrahydate (99%) and Fe (III) chloride hexahydrate (97%) were purchased from Acros. Copper (II) sulfate pentahydrate ($CuSO_4{\cdot}5H_2O$) was purchased from Merck (Darmstadt, Germany). Sodium hyaluronate (HA) was purchased from Shandong Freda Biochem. Co. (China). 1,2-Distearoyl-sn-glycero-3-phosphocholine (DSPC) was purchased from Avanti Polar Lipids, Inc. (USA). Methoxypolyethylene glycol amine (MPEG-NH_2) (M.W. = 5000), 1-ethyl-3-(3-dimethylaminopropyl)carbodiimide (EDC), potassium thiocyanate (KSCN), 4-morpholineethanesulfonic acid monohydrate (MES monohydrate), dimethyldioctadecyl ammonium bromide (DDAB), cholesterol (CH), ICG and Triton X-100 were purchased from Sigma-Aldrich Co. (USA). All other chemicals were of reagent grade and used without further purification.

2.2. Synthesis of citric acid coated iron oxide magnetic nanoparticles (CMNPs)

The CMNPs were prepared by the chemical precipitation method as described before with slight modification [24]. Briefly, MNPs were first prepared by dissolving 0.875 g $FeCl_2$ and 2.375 g $FeCl_3$ (Fe^{2+}:Fe^{3+} = 1:2) in 40 mL of double-distilled water (DDI water) in a three-neck flask and continuously stirred at 100 rpm in the presence of nitrogen gas for 15 min at 70 °C–80 °C. After increasing the stirring rate to 1100 rpm, 5 mL NH_4OH (28%) was added to the flask and stirred for

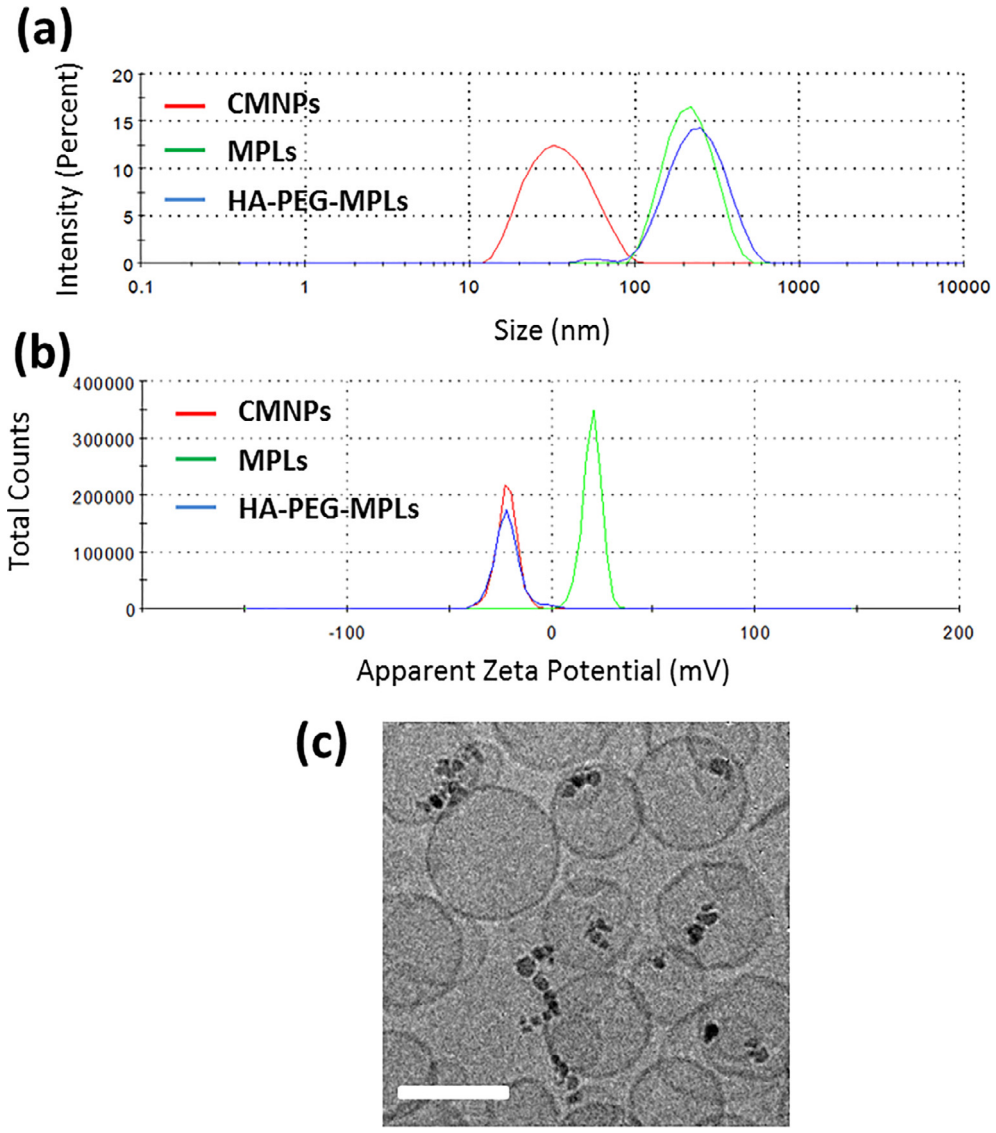

Fig. 2. (a) Particle size distribution from dynamic light scattering and (b) apparent zeta potential distribution of CMNPs, MPLs and HA-PEG-MPLs. (c) cryo-TEM image of HA-PEG-MPLs with CMNP agglomerates (black dots) entrapped inside the liposomes (bar = 200 nm).

Table 1
Particle size and zeta potential of CMNPs, MPLs and HA-PEG-MPLs. The data are expressed as means ± standard deviations (n = 6).

Sample	Particle Size (nm)	Polydispersity index	Zeta Potential (mV)
CMNPs	31.4 ± 3.3	0.22 ± 0.02	−21.7 ± 3.4
MPLs	195.0 ± 20.6*	0.26 ± 0.04*	19.4 ± 4.7*
HA-PEG-MPLs	221.9 ± 16.9*	0.29 ± 0.03*	−20.0 ± 4.2*,#

* $p < 0.05$ compared with CMNPs.
\# $p < 0.05$ compared with MPLs.

additional 30 min. To coat citric acid on MNPs, the temperature of the solution was increased to 95 °C and citric acid (1 mg/mL) was added drop by drop. The reaction was allowed to proceed further for 90 min. After cooled down to room temperature, the solution was diluted to twice its volume with DDI water and subject to magnetic separation with a permanent magnet for 10 min. The supernatant containing CMNPs was continuous washed with 0.5 L of DDI water in a 30 kDa molecular weight cut-off (MWCO) hollow fiber module (Spectrum Laboratories) to remove excess citric acid and NH_4OH.

2.3. Synthesis of HA-PEG

HA-PEG was synthesised according to the method described before [25] with some modification. 1.2 g (1 μmol) of HA and 5 mg MPEG-NH_2 (1 μmol) were mixed in 100 mL of 50 mM MES monohydrate buffer (pH 6.5). To this solution, 0.192 g (1 mmol) of EDC was added and allowed to react for 12 h at room temperature. The solution was dialyzed against DDI water for 48 h at room temperature to remove excess MPEG-NH_2 with 10 kDa MWCO dialysis tubing.

2.4. Preparation of liposomes

Magnetic photosensitive liposomes (MPLs) were prepared by using solvent evaporation, hydration, sonication and extrusion [26,27]. Lipid mixtures of DSPC, CH and DDAB (molar ratio 5:3:1) were taken in a round-bottom flask. This mixture was dissolved in chloroform/methanol solution (2:1, v/v). The organic solvent was removed using a rotary evaporator (EYELA N-1200AVF, Japan) at 100 psi and 54 °C with a water bath for 20 min. The solvent was then completely removed in a vacuum oven overnight to form a thin phospholipid film on the wall of the round-bottom flask. The resulting dry thin film was re-hydrated with a phosphate buffer (10 mM, pH 7.4) solution containing CMNPs

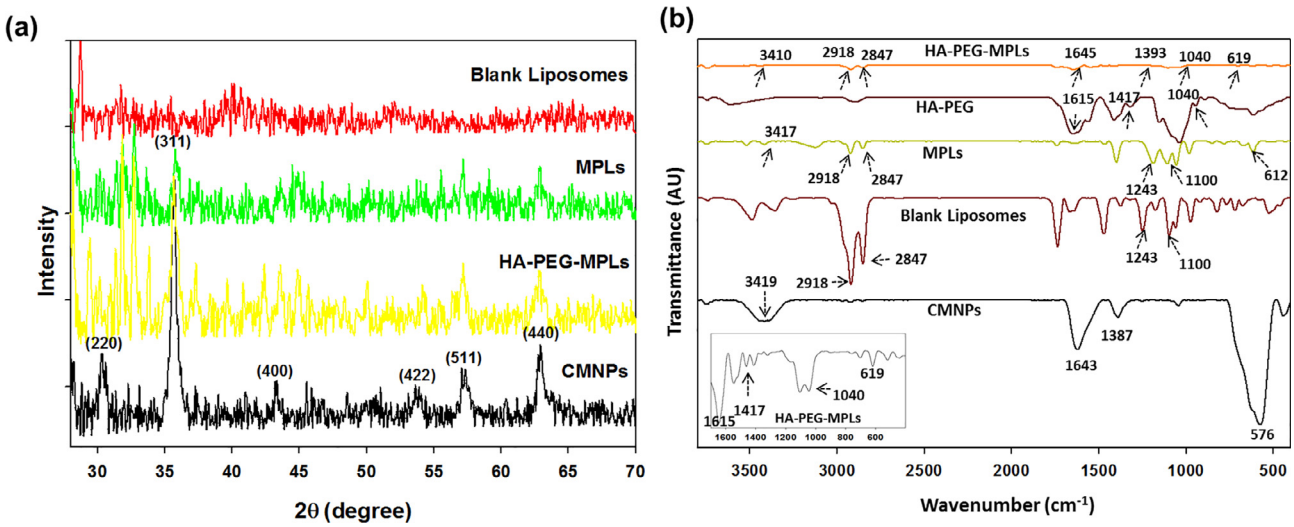

Fig. 3. Characterization of different samples by X-ray diffraction (XRD) (a) and Fourier transform infrared (FTIR) (b).

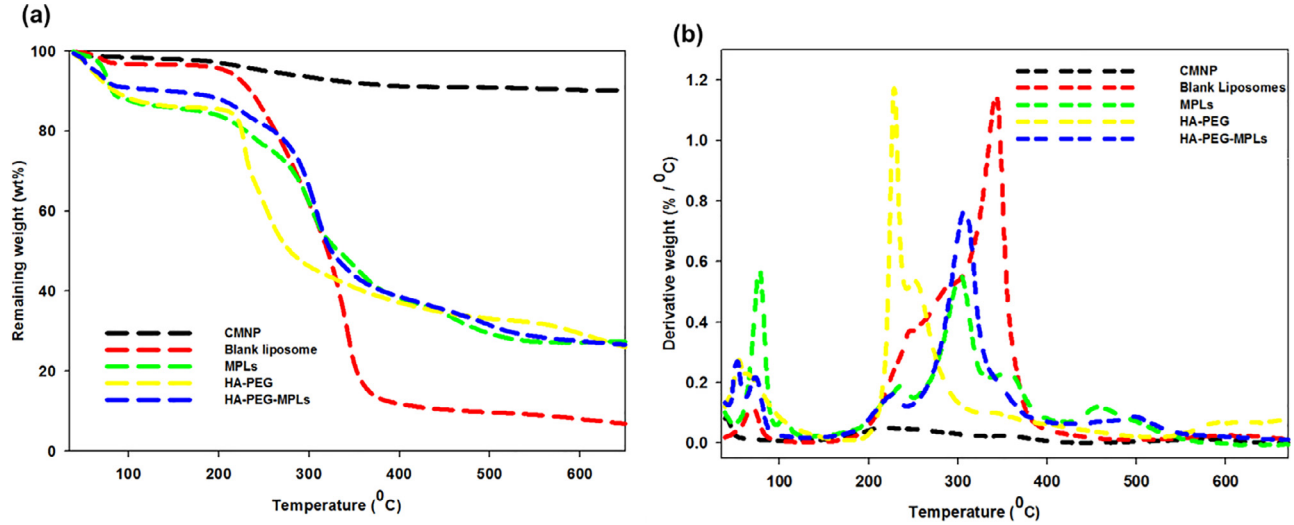

Fig. 4. Characterization of different samples by thermogravimetric analysis (TGA) (a) and differential thermal analysis (DTA) (b).

(0.3 mg/mL), ICG (50 μg/mL), and $CuSO_4{\cdot}5H_2O$ (300 mM) for 20 min at 54 °C. The hydrated solution was then sonicated for 15 min. After sonication, the MPLs were extruded for 20 cycles using double-stacked polycarbonate membranes with 0.2 μm pore size (Whatman, NJ, USA) in a commercial temperature-controlled barrel extruder (Lipex® Extruder, TRANSFERRA Nanosciences Inc., Canada). The un-encapsulated CMNPs were removed by centrifugation for 10 min at 1000*g*. The resulted solution was ultra-centrifuged for 30 min at 60,000*g*. For preparation of HA-PEG-MPLs, MPLs solution in distilled water (1 mg/mL) were sonicated for 10 min before adding HA-PEG (0.5 mg/mL) dropwise and gently shaken at 4 °C overnight. The HA-PEG-MPLs solution was centrifuged to remove excess HA-PEG at 45,000*g* for 20 min at 20 °C and re-suspended in distilled water by sonicating for 5 min. Blank liposomes without MNPs and ICG were similarly prepared for comparison.

2.5. Determination of encapsulation efficiency of CMNPs and ICG

The amount of CMNPs in MPLs was determined by a spectrophotometric method [27]. Briefly, to 40 μL of MPLs solution, 10 μL of Triton X-100 (1% v/v) was added and incubated for 10 min at 43 °C. Then, 450 μL HCl (37%) and 500 μL of 40 mM KSCN were added to the samples and incubated for 5 min. The absorbance of the solution was measured at 480 nm in a UV–VIS Spectrophotometer. The CMNPs concentration was then determined from a standard curve prepared beforehand. The ICG concentration was determined from the absorbance of MPLs in 80% methanol at 785 nm with a standard curve [28]. The encapsulation efficiency (EE) and loading efficiency (LE) of CMNPs and ICG was calculated using the following equations.

$$\text{EE (\%)} = \frac{\text{Weight of encapsulated CMNPs or ICG}}{\text{Weight of CMNP or ICG initially added}} \times 100 \quad (1)$$

$$\text{LE (\%)} = \frac{\text{Weight of encapsulated CMNPs or ICG}}{\text{Weight of liposomes}} \times 100 \quad (2)$$

2.6. Characterization of HA-PEG-MPLs

The particles size and zeta potential of CMNPs, MPLs and HA-PEG-MPLs were determined by dynamic light scattering (DLS) using a Zetasizer Nano ZS (Malvern Instruments Ltd., Worcestershire, UK). The DLS analysis was performed at a scattering angle of 173° at 25 °C in the auto-measuring mode. Particles dispersions were diluted with DDI water for measurements. The structure of CMNPs in HA-PEG-MPLs was observed by cryogenic transmission electron microscopy (cryoTEM). The cryo-fixed specimens were mounted into a Gatan cryo-holder

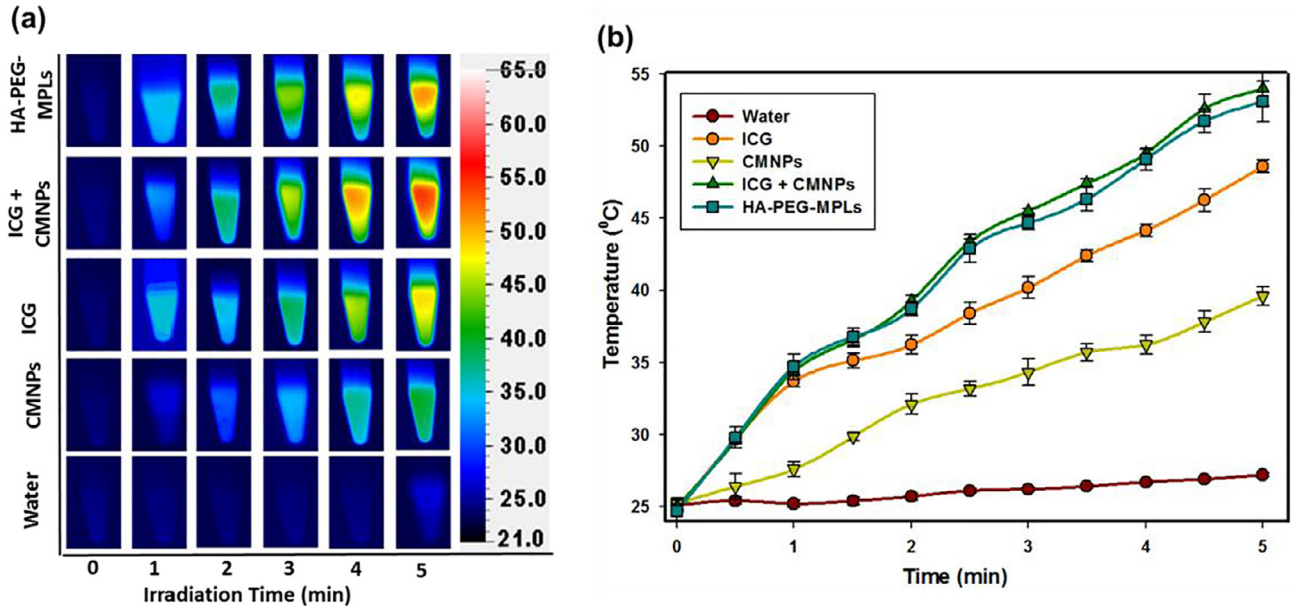

Fig. 5. The ex vivo photothermal effects from infrared thermal camera images (a) and peak temperature profiles (b) for HA-PEG-MPLs, ICG + CMNPs, CMNPs, ICG and water with continuous NIR laser irradiation (808 nm, 2.0 W/cm^2 for 5 min).

(Model 914, Gatan Inc.) for direct observation at −170 °C at 120 kV using a JEOL JEM-1400 TEM (Tokyo, Japan). Thermogravimetric analysis (TGA) was conducted with 8–10 mg of powder sample in nitrogen atmosphere from 25 to 750 °C, with a heating rate of 10 °C/min using a Q50 TGA from TA Instruments (New Castle, DE, USA). For Fourier transform infrared spectroscopy (FTIR) spectrum, the sample was blended with KBr, compressed to form a pellet and analyzed with a TENSOR II FTIR spectrometer (Bruker Optics Inc., Billerica, MA, USA). The transmission spectra were obtained from 400 to 4000 cm^{-1} at 2.5 mm/s with a resolution of 4 cm^{-1}. For X-ray diffraction (XRD) analysis of the crystallographic characteristic of samples, a D2 Phaser X-ray powder diffractometer (Bruker, WI, USA) was used by scanning in the 2θ range of 20–70° with CuKα radiation. The crystalline grain size was determined from the strongest plane (3 1 1) reflection peak using the Debye-Scherrer equation.

$$D = \frac{\kappa\lambda}{\beta\cos\theta} \quad (3)$$

where κ is dimensionless shape factor, close to unity, normally taken as 0.9, λ is the wavelength of X-ray, β is full width at half max (FWHM) of the diffraction peak, θ is the Bragg angle and D is the average size of the crystalline domains.

2.7. Temperature elevation induced by NIR laser irradiation

The temperature profile of different samples after exposure to laser irradiation was determined from thermal images captured with a thermal camera (InfReC Thermo GEAR G100EX, Nippon Avionics Co., Tokyo, Japan). Aqueous suspension of HA-PEG-MPLs, mixture of ICG and CMNPs, ICG, CMNPs and distilled water in Eppendorf tube (0.5 mL) were irradiated by NIR 808 nm laser at 2 W/cm^2 for 5 min. The amount of ICG in the solution was kept constant for ICG, mixture of ICG and CMNPs and HA-PEG-MPLs samples (6.53 μg/mL) while the amount of CMNPs was fixed at 282 μg/mL for CMNPs and HA-PEG-MPLs samples [14,29]. The temperatures of the solutions were monitored at 30 s intervals.

2.8. In vitro cell culture experiments

For in vitro cytotoxicity tests, 2.5 × 10^3 U87MG cells were seeded to each well of a 96-well cell culture plate and cultured in Dulbecco's Modified Eagle Medium (DMEM) supplemented with 10% fetal bovine serum overnight in a humidified CO_2 incubator at 37 °C under 5% CO_2 atmosphere. The cell culture medium was replaced with HA-PEG-MPLs of various concentrations in DMEM and incubated at 37 °C for 10 h in a humidified CO_2 incubator for intracellular uptake of HA-PEG-MPLs. The medium in each well was then completely removed and replaced with fresh medium. Each well was exposed to 808 nm NIR laser light at 2 W/cm^2 for 4 min [30]. After irradiation, the plate was incubated again for 30 min before determining cell viability by MTT assays with 3-(4,5-dimethylthiazol-2-yl)-2,5-diphenyltetrazolium bromide using a microplate reader at 540 nm. Live/Dead cell assays were performed with U87MG cells to verify the photothermal effects by using 1 × 10^4 U87MG cells in 24-well cell culture plates. After treatment with HA-PEG-MPLs at 2 mg/mL in DMEM at 37 °C for 10 h, the existing medium in the well was replaced with fresh medium and each well was irradiated with 808 nm NIR laser at 2 W/cm^2 for 4 min. After irradiation, the plate was incubated again for 30 min before staining with calcein AM/ethidium homodimer in the LIVE/DEAD™ Viability/Cytotoxicity Kit for mammalian cells (Thermo Fisher Scientific) and observed under an inverted fluorescence microscope (Olympus IX-71, Tokyo, Japan). The temperature profiles in the cell culture plate after exposure to laser irradiation was also monitored from thermal images captured with a thermal camera (InfReC Thermo GEAR G100EX, Nippon Avionics Co., Tokyo, Japan).

2.9. In vivo antitumor efficacy

Female BALB/c nude mice weighing approximately 15–20 g (4–6 weeks old) were purchased from the National Laboratory Animal Center (Taipei, Taiwan). All animal experiments were conducted according to protocols approved by the Institutional Animal Care and Use Committee of Chang Gung University. To establish the xenograft tumor model, 1 × 10^6 U87MG cells were administered by subcutaneous injection into the right flank of the nude mice at day 0. When the tumor volumes had grown to approximately 50–80 mm^3 (day 10), mice were randomly divided into three groups (4 mice in each group) for treatment. Group 1: intravenous injection with 200 μL of saline (control) at day 10, 14, 17 and 20; group 2: intravenous injection with 200 μL of saline at day 10, 14, 17 and 20 and irradiation with 808 nm laser at

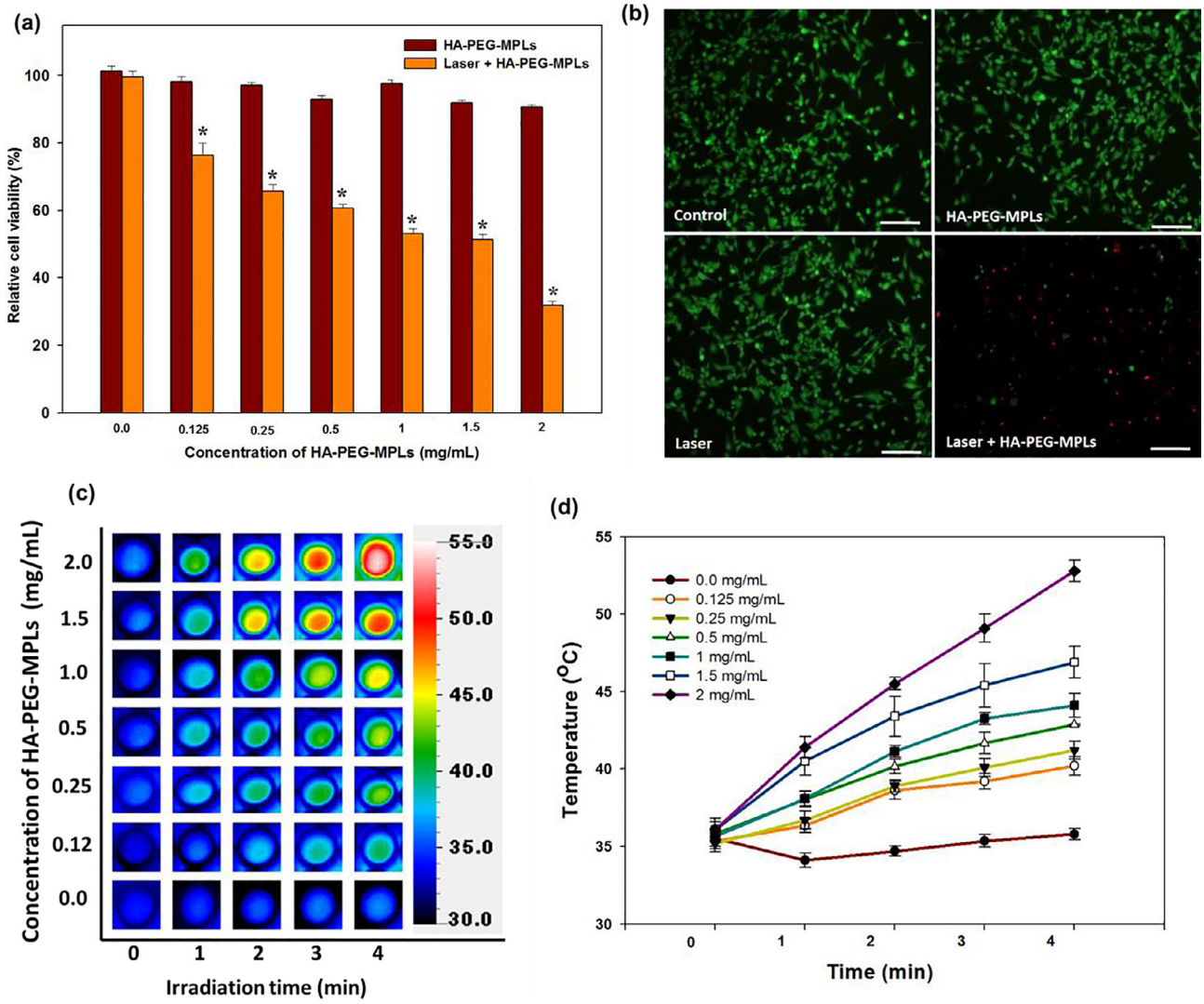

Fig. 6. The in vitro cell cytotoxicity and live/dead cell assays. (a) Relative viability of U87MG cells incubated 10 h with different concentrations of HA-PEG-MPLs with or without 808 nm laser irradiation (2 W/cm^2 for 4 min) (n = 5). * $p < 0.05$ compared HA-PEG-MPLs. (b) Fluorescence microscopy images of U87MG cells incubated 10 h with HAPEG-MPLs (2 mg/mL) and exposed to the 808 nm laser irradiation (2 W/cm^2 for 4 min). Live and dead cells were stained with calcein AM (green color) and ethidium homodimer-1 (red color), respectively. Bar = 100 μm). The temperature profile images captured with an infrared thermal camera (c) and peak temperature profiles (d) are shown for different liposome concentrations used for cell culture. (For interpretation of the references to colour in this figure legend, the reader is referred to the web version of this article.)

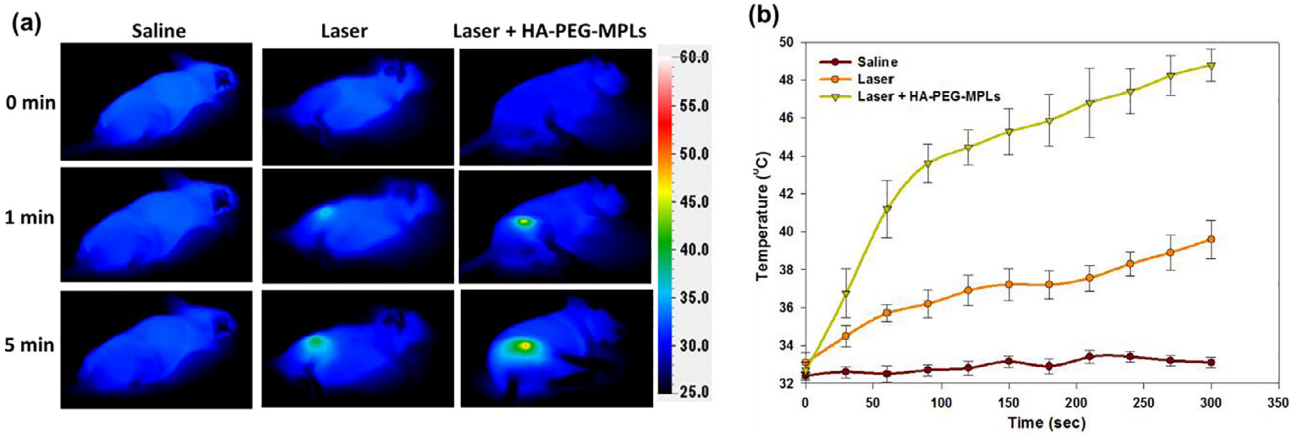

Fig. 7. In vivo photothermal effects of tumor-bearing mice after injection with saline, injection with saline followed by NIR laser irradiation (808 nm at 2.0 W/cm^2) and injection with HA-PEG-MPLs followed by NIR laser irradiation (808 nm at 2.0 W/cm^2). (a) IR thermal images showing the temperature changes in tumor areas of mice after different treatments. (b) Peak temperature profiles in tumors after different treatments.

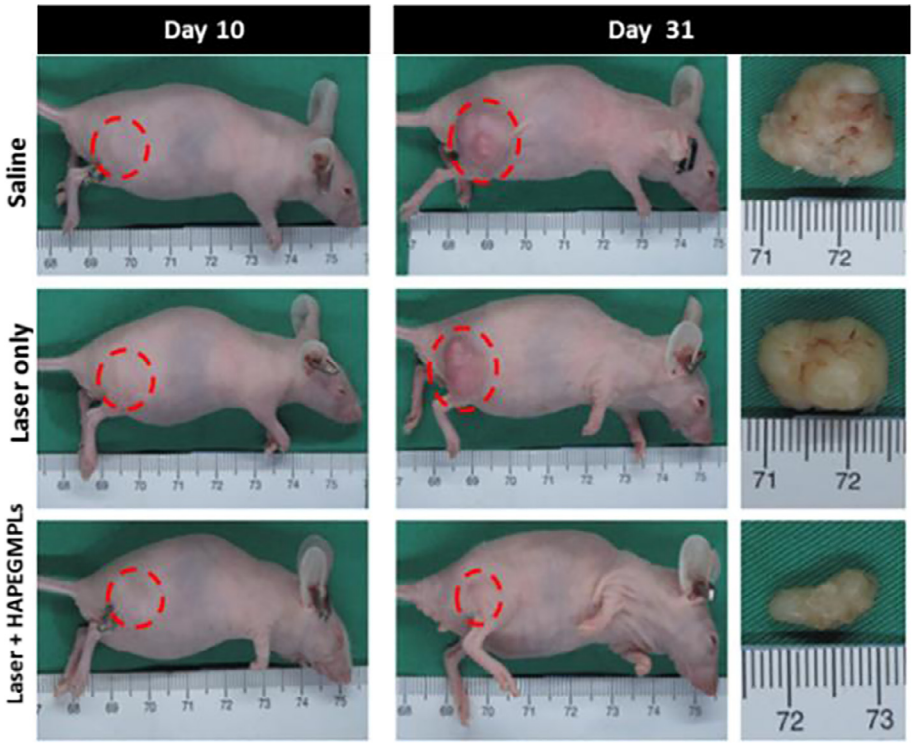

Fig. 8. Representative photographs of the tumor-bearing 10 days and 31 days post-implantation of U87MG tumor cells. Treatment started on day 10. The retrieved tumors on day 31 were also shown for each group.

2.0 W/cm^2 for 5 min after each injection (laser); group 3, intravenous injection with 200 µL of HA-PEG-MPLs (3 mg/mL) at day 10, 14, 17 and 20, followed by placing a permanent magnet (1400 Gauss) at the vicinity of the tumor site for 90 min and irradiation with 808 nm NIR laser at 2.0 W/cm^2 for 5 min after each injection (laser + HA-PEG-MPLs). The temperature distribution around the tumor area was determined form thermal images captured with an infrared thermal camera (Thermo GEAR G100EX, Tokyo, Japan). The body weight and tumor size was continuously monitored twice a week. The tumor size was measured using a calliper, from which the tumor volume was calculated according to the length and width of the tumor as length × (width)^2/2 [14,31]. For ethical reasons, animals were euthanized when the volume of the implanted tumor reached 1 cm^3 and the survival curve was determined from the remaining mice.

For histological analysis, one mouse from each group was sacrificed at day 34. The tumor was harvested immediately from the animal and preserved in formaldehyde. The tumor tissue was treated with 10% phosphate buffered formalin, followed by paraffin-embedment and sectioned into ~5 µm thickness for hematoxylin and eosin (H&E) staining. For immunohistochemical (IHC) staining, the paraffin-embedded tumor tissue was stained for the cell proliferation marker Ki-67 with the UltraVision™ Quanto Detection System HRP DAB (Thermal Fisher Scientific) and counterstained with hematoxylin. The primary antibody used was rabbit anti-Ki-67 monoclonal antibody from Thermal Fisher Scientific (MA5-14520).

2.10. In vivo IVIS imaging

Since the U87MG glioblastoma cell line was genetically engineered to express the firefly luciferase gene [32], we used bioluminescence imaging to evaluate the anti-tumor efficacy based on the bioluminescence intensity (BLI) from each mouse. At day 14, 18, 24 and 27 post-implantation, 0.1 mL of luciferase (15 mg/mL) was injected intraperitoneally into the mouse and bioluminescence imaging was performed using non-invasive in vivo imaging system (IVIS) (Xenogen IVIS-200, Caliper Life Sciences, Hopkinton, MA, USA). The BLI was determined at baseline at day 10 (i.e. before treatment) and at each time point after treatment by measuring the total peak BLI through standardized regions of interest (ROIs) in tumor by using the Living Image® 4.0 software. The normalized BLI was calculated from the total bioluminescent signal intensity at each time point after normalizing by the total signal intensity at baseline. To study the tumor-targeting ability of HA-PEG-MPLs, tumor-bearing mice were injected intravenously with 200 µL of HA-PEG-MPLs (3 mg/mL) or 200 µL saline intravenously. Magnetic guidance was achieved by an external magnetic field (1400 Gauss) for 2 h and fluorescence imaging was carried out with IVIS at 745 nm/850 nm excitation/emission wavelength for detection of ICG.

2.11. Statistical analyses

All data were subjected to analysis one-way analysis of variance (ANOVA) and reported as mean ± standard deviation (SD). Turkey's post-hoc test was used to determine the difference between any two groups with p value < 0.05 considered to be statistically significant.

3. Results and discussion

3.1. Characterization of HA-PEG-MPLs

We first coated HA-PEG to MPLs, which entrap ICG and MNPs, to fabricate HA-PEG-MPLs similar to the layer-by-layer technology where multilayer films of oppositely charged polyelectrolytes were coated alternatively to liposomes [33]. The distribution of hydrodynamic diameters and zeta potentials of CMNPs, MPLs and HA-PEG-MPLs are shown in Fig. 2a and b while their average values are compared in Table 1. As MPLs are formed from DDAB, they are cationic liposomes and have a positive zeta potential. As HA is an anionic glycosaminoglycan while PEG does not contained any charged groups, the zeta potential of liposomes shifted from 19.4 mV for MPLs to −20.0 mV for

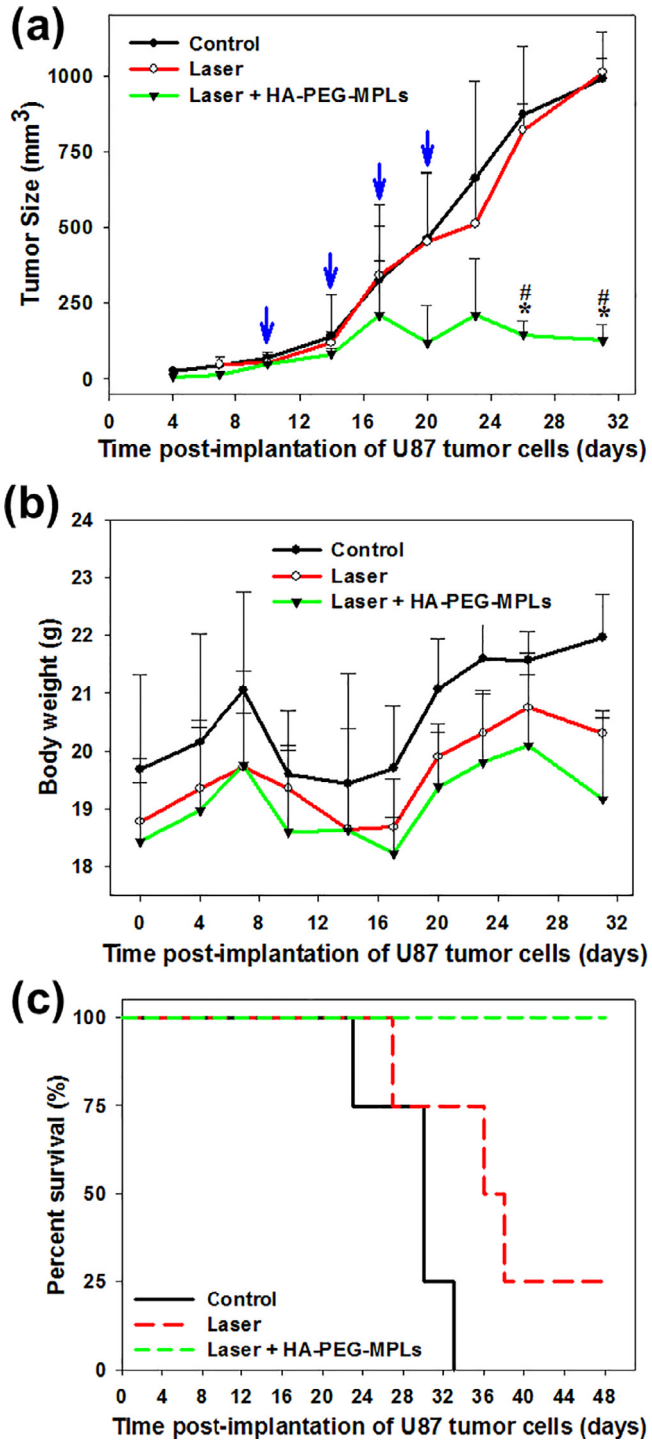

Fig. 9. The tumor volume (a), body weight (b) and survival curve (c) after different treatments. The blue arrows in (a) indicated the times for laser irradiation in the laser and laser + HA-PEG-MPLs groups (2.0 W/cm^2 for 5 min). The mice were sacrificed when the tumor volume reached 1000 mm^3, from which survival curves were calculated (c).

HA-PEG-MPLs, which confirms that HA-PEG is successfully coated onto the surface of MPLs through ionic interactions. There is no statistical difference in average particle size between MPLs and HA-PEG-MPLs, indicating the self-assembly of HA-PEG on MPLs provide a simple yet efficient method to introduce HA as a targeting ligand. In addition, PEG could be introduced together with HA to extend blood-circulation time of HA-PEG-MPLs while minimizes the clearance by the reticuloendothelial system (RES) when macrophages in the RES located in the liver and the spleen vividly take up particles bound with serum proteins, which could be reduced by surface modification by PEG [34]. The restriction of the particle size of HA-PEG-MPLs to ~220 nm will also improve the enhanced permeability and retention (EPR) effect as the nano-sized vehicle with long circulation times could leak preferentially into tumor tissue through a leaky tumor vasculature and be retained in the tumor bed due to reduced lymphatic drainage [35]. The structures of HA-PEG-MPLs characterized by cryo-TEM showed agglomerate of discrete CMNPs of ~15 nm size in the aqueous core surrounded by a lipid bilayer and with a particle size consistent with that from DLS measurements (Fig. 2c). For encapsulation efficacy, the EE value was 91.7 ± 2.1% for CMNPs and 12.1 ± 3.8% for ICG while the LE value was 13.5 ± 2.3% for CMNPs and 0.38 ± 0.10% for ICG.

Fig. 3a shows X-ray diffraction (XRD) patterns of CMNPs, MPLs and HA-PEG-MPLs in comparison with that of blank liposomes (liposomes prepared similarly but without CMNPs and ICG). For CMNPs, MPLs and HA-PEG-MPLs, six diffraction peaks at 2θ = 30.2°, 35.4°, 43.2°, 53.4°, 57.2° and 62.7° could be indexed to the (2 2 0), (3 1 1), (4 0 0), (4 2 2), (5 1 1), and (4 4 0) planes of a cubic cell. The crystalline structure of the particle can be confirmed to correspond to that of a magnetite structure (JCPDS card number 19–0629), confirming that all resultant nanoparticles were pure Fe_3O_4 with a cubic spinal structure of the magnetite [24,31,36]. This could be further confirmed from the XRD patterns observed for blank liposomes, where no diffraction peaks corresponding to CMNPs could be observed. It is also evident that co-encapsulation of CMNPs with ICG in liposomes did not lead to change in the crystalline phase of CMNPs. The average crystal grain size calculated from the Scherrer equation is from 13.3 to 15.1 nm from the strongest (3 1 1) diffraction peak for all CMNPs-containing samples.

In Fig. 3b, the FTIR analysis of CMNPs showed the strongest peak at 3419 cm^{-1}, indicating the presence of −OH vibrations. The peak at 576 cm^{-1} indicated the existence of Fe−O stretching bond in the nanoparticles [37]. The characteristic peaks of citric acid at 1394 and 1735 cm^{-1}, due to the symmetric vibration and asymmetric stretching of C−O from −COOH group and C═O from −COOH, were shifted to 1387 and 1643 cm^{-1} in CMNPs, respectively. This observation is a direct evidence to support that citric acid was coated onto the surface of MNPs via chemisorption of carboxylate groups. In blank liposomes, the characteristic peaks of DSPC showed the CH_2 symmetric and asymmetric stretch modes at 2847 cm^{-1} and 2918 cm^{-1}, while the phosphate group (P═O) of symmetric and asymmetric stretch modes showed characteristic peaks at 1100 cm^{-1} and 1243 cm^{-1} [38,39]. For MPLs the strongest bands at 2918 cm^{-1} and 2847 cm^{-1} represented the CH_2 symmetric and asymmetric stretch modes. Also, the characteristic peaks at 612 cm^{-1} and 3417 cm^{-1} corresponding to the Fe−O stretching and −OH vibrations of CMNPs confirmed the existence of CMNPs inside the liposomes. In the spectrum of HA-PEG, the absorption peaks at 1615 cm^{-1} and 1417 cm^{-1} represented the symmetric and asymmetric stretching vibration bands of the carboxyl group while the peak at 1040 cm^{-1} could be attributed to the C−O−C stretching [23,40]. In the FTIR spectrum of HA-PEG-MPLs, all expected and existing peaks existed, with specific reference to the peaks assigned to HA-PEG (shown in the enlarged spectrum in the insert of Fig. 3b), suggesting that HA-PEG is successfully coated on MPLs to form HA-PEG-MPLs as driven by ionic interactions.

The thermogravimetric analysis (TGA) and differential thermal analysis (DTA) curves of CMNPs, blank liposomes, MPLs, HA-PEG and HA-PEG-MPLs were shown in Fig. 4. A ~10% weight loss was observed at 700 °C in CMNPs due to thermal decomposition of −OH functional groups [31,41]. For blank liposomes, after an initial weight loss due to water, substantial weight loss (~85%) from 240 °C to 380 °C was observed with a decomposition peak temperature at ~340 °C to result in ~8% residual weight at 700 °C. In contrast, MPLs showed higher thermal stability and less weight loss (74%) due to CMNPs in the liposomes and the peak decomposition temperature shifted to 300 °C. For HA-PEG, the early weight loss from 60 °C to 100 °C represents the

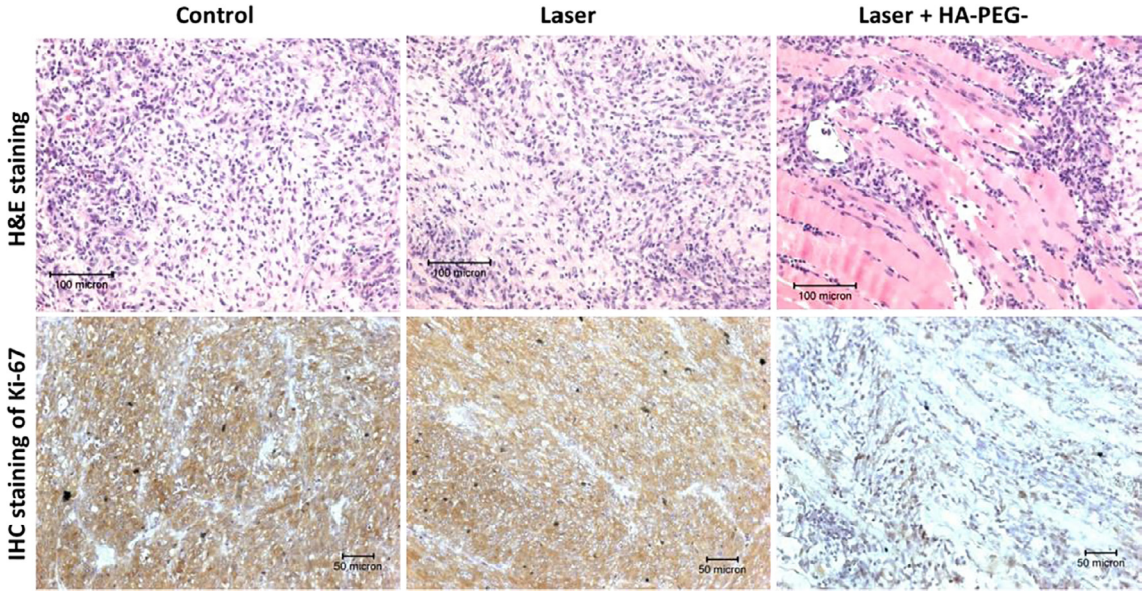

Fig. 10. H&E (bar = 100 μm) and immunohistochemical (IHC) staining of Ki-67 (bar = 50 μm) of tumor sections after different treatments 34 days post-implantation of U87MG tumor cells.

vanishing of residually bound water mostly to HA. A thermal decomposition started from 200 °C to 280 °C with the maximum weight loss peak at 251 °C and weight loss of ~72% after reaching 700 °C [23]. Considering HA-PEG-MPLs, the DTA curve showed all decomposition peaks due to MPLs (300 °C) and HA-PEG (251 °C) and showed similar weight loss (~73%) to MPLs, confirming the encapsulation CMNPs in HA-PEG-MPLs and HA-PEG coating on HA-PEG-MPLs.

3.2. Ex vivo photothermal effects of HA-PEG-MPLs

The photothermal effect of HA-PEG-MPLs was first studied when solutions of HA-PEG-MPLs, ICG, CMNPs and ICG + CMNPs at the same concentrations of ICG and CMNPs (6.53 μg/mL ICG and 282 μg/mL CMNPs) were exposed to 808 nm laser light irradiation at 2.0 W/cm^2 up to 5 min. The temperature rise as a function of light exposure time was monitored using an infrared thermal camera (Fig. 5). There was no obvious temperature change observed when distilled water was exposed to NIR laser. In comparison, under the same laser irradiation conditions, the solution temperature reached 55.2 °C, 54 °C, 49 °C and 38 °C for HA-PEG-MPLs, ICG + CMNP, ICG and CMNPs, respectively. The combinations of ICG and CMNPs could enhance the photothermal effect from ICG or CMNP alone. In addition, HA-PEG-MPLs and ICG + CMNPs showed comparable temperature profiles, indicating their encapsulation in HA-PEG-MPLs does not lead to diminished photothermal efficacy. Considering the thermal effects of CMNPs, magnetic hyperthermia of Fe_3O_4 MNPs produced via dipole relaxation is usually achieved under an alternating magnetic field [42]. Nonetheless, the technique requires high current and voltage due to large air volume within the applied field in which energy cannot be easily focused. Only very recently, NIR light induced photothermal effect for Fe_3O_4 MNPs has been reported for its good photothermal converting efficiency for photothermal ablation of tumors [43]. Taken together, ICGs and CMNPs showed photothermal effects, endorsing HA-PEG-MPLs to be an effective photothermal nano-agent for PTT.

3.3. In vitro cytotoxicity of HA-PEG-MPLs

To examine the cytotoxicity of HA-PEG-MPLs against tumor cells, U87MG cells were contacted with HA-PEG-MPLs of different concentrations for 10 h before irradiation with 808 nm NIR laser at 2 W/cm^2 for 4 min. The cell viability was determined through MTT assays. As shown from Fig. 6a, U87MG cells exposed to the laser light showed significant difference in cell viability compared with those without laser irradiation at every HA-PEG-MPLs concentration. The enhanced cytotoxicity toward U87MG is also dose-dependent on HA-PEG-MPLs concentrations. In contrast, no obvious decrease in cell viability was observed upon exposure to HA-PEG-MPLs at all concentrations but without laser irradiation. This photothermal effect of HA-PEG-MPLs was further confirmed from the live/dead cell assays where live and dead U87MG cell could be identified by staining with calcein AM and ethidium homodimer-1, respectively. As shown in Fig. 6b, treatment with HA-PEG-MPLs or laser irradiation alone did not influence the cell viability from the control judging from the abundance of live cells (green fluorescence) with no observable dead cells (red fluorescence). In contrast, laser + HA-PEG-MPLs treatment led to a drastic change in fluorescence signals where minimum live cells together with abundant dead cells were observed. The empty space observed for this group may be occupied by dead cells that were detached from the surface of the cell culture plate during the washing step. Indeed, those results underlines that either laser or HA-PEG-MPLs alone did not lead to killing of cancer cells but only HA-PEG-MPLs plus laser irradiation could effectively lead to PTT/PDT dual mode killing of cancer cells. Fig. 6c and d show the temperature increase in the cell culture plate after laser irradiation is correlated with the increase of liposome concentration for cell culture, which results in lower cell viability as shown in Fig. 6a due to increased intracellular liposome concentration.

3.4. In vivo effects of HA-PEG-MPLs

To study the efficiency of HA-PEG-MPLs for in vivo cancer therapy, xenograft tumor model in nude mice was established by subcutaneously implanted U87MG cells. Ten days post-implantation, when the tumor size reached 50–80 mm^3, different treatments were started. The photothermal effect of the tumor-bearing mice in vivo was first monitored with an infrared thermal camera as shown Fig. 7a. There was no temperature increase found after 5 min for the control group injected with saline. In the group injected with saline and treated with laser, in contrast with the ex vivo photothermal effect observed in Fig. 5, there was a slight increase in temperature from 33.1 °C to 39.6 °C in 5 min (Fig. 7b). However, this slight increase in temperature would not lead to tumor destruction as magnetic hyperthermia for cancer treatment involved temperatures from 41 °C to 46 °C [44]. In the group injected

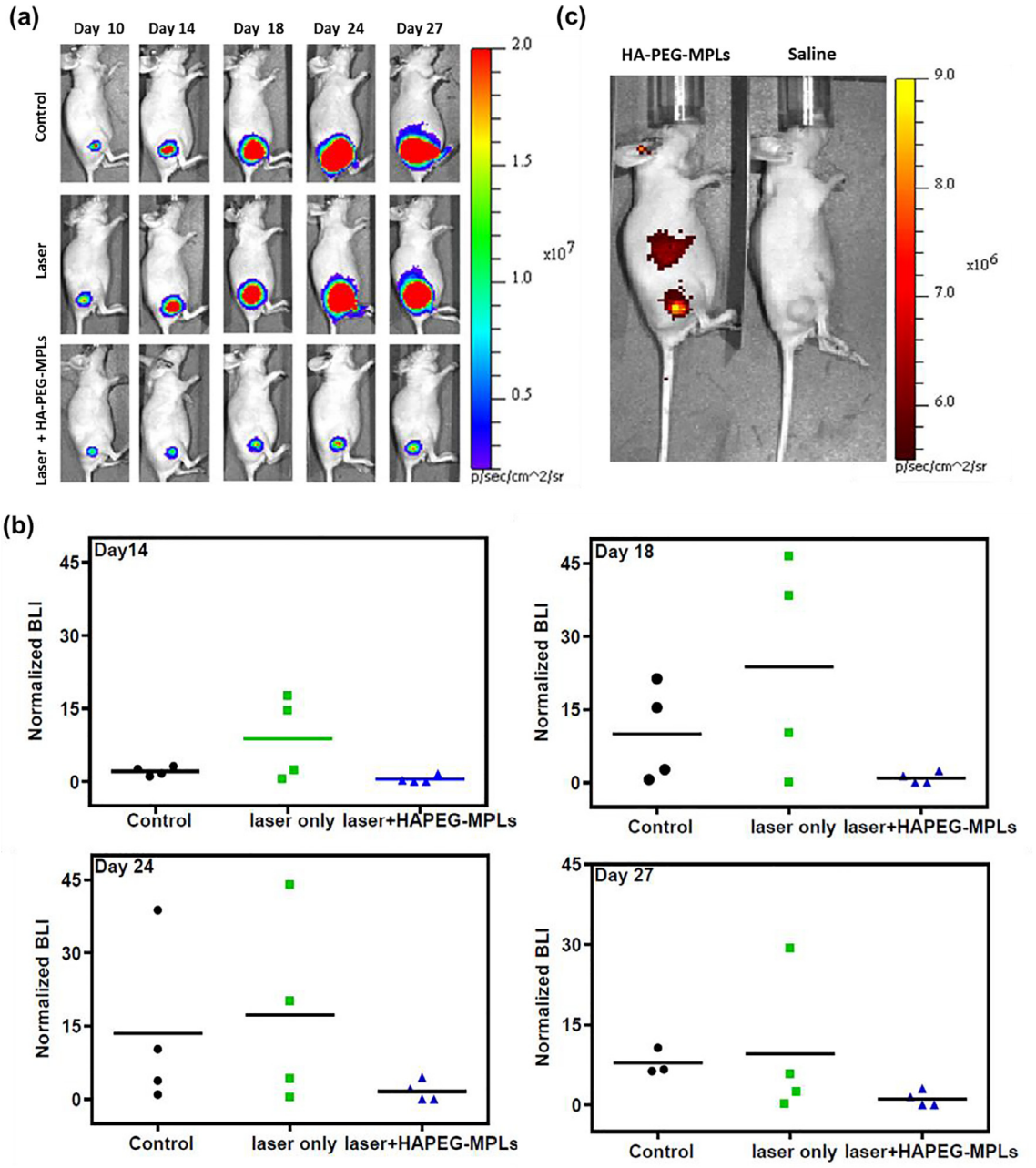

Fig. 11. The in vivo bioluminescence and fluorescence imaging by IVIS. The anti-tumor efficacy was shown from the bioluminescence imaging pictures (a) and the normalized bioluminescence intensity (BLI) at different time points after different treatments (b). For targeting effects, the fluorescence imaging pictures 2 h after injection with HA-PEG-MPLs or saline are shown in (c).

with HA-PEG-MPLs combined with laser irradiation, there is a rapid increase in temperature from 32.9 °C to 42.7 °C within 1 min and then reaching 49.3 °C in the next 4 min (Fig. 7b).

Gross images of the tumor-bearing mice on day 10 (treatment started) and day 31 post-implantation of U87MG cells demonstrated the apparent tumor size difference of the laser + HA-PEG-MPLs group from the other two groups with tumors removed from the animals on day 31 supporting the excellent anti-tumor effects (Fig. 8). The tumor volume was recorded every 3 days from day 0 to day 31. The tumor volume increased rapidly with time for the control and laser groups (Fig. 9a). However, the tumor volume in the laser + HA-PEG-MPLs group remained below 150 mm^3 throughout the observation period. Specifically, the tumor volumes of the control and laser groups were 7.7–7.9 times that of the laser + HA-PEG-MPLs group at the end of the observation period (day 31).

The mice did not exhibit any significant difference in body weights between groups (Fig. 9b). However, mice in the control group without laser treatment showed a trend of better weight gain compared to other groups with laser treatment, which is consistent with the general perception that laser exposure leads to weight loss. The mouse was sacrificed when the tumor volume reached 1000 mm^3 and survival curve was constructed form the percentage of remaining mice in each group (Fig. 9c). The mean survival times for the control and laser groups were 30 and 36 days, respectively. In contrast, all mice in the laser + HA-PEG-MPLs group survive throughout experiment period up to 48 days post-implantation of tumor cells. Taken together, the remarkable cancer treatment efficacy was achieved by PDT/PTT from the laser + HA-PEG-MPLs group.

Based on results of H&E staining of tumor tissue on day 31, no evidence of necrosis was observed for the control and laser groups

(Fig. 10). In contrast, cavitation phenomenon in coagulative necrosis was observed in the laser + HA-PEG-MPLs group. Cancer therapy should also inhibit proliferation of cancer cells from histology of tumor tissue. The Ki-67 protein is used as a proliferation marker in tumor specimens and its IHC expression has prognostic and predictive value in cancer [45]. The IHC staining of tumor sections associated with Ki-67 protein in Fig. 10 clearly indicated that a greater number of actively proliferating tumor cells existed in tumor sections from the control and the laser groups. In contrast, the tissue sections from the tumor treated with laser + HA-PEG-MPLs showed very weak Ki-67 immunoreactivity and minimum Ki-67 protein production. Therefore, we conclude that laser + HA-PEG-MPLs can provide effective anticancer activity to effectively inhibit proliferation of cancer cells.

3.5. *In vivo antitumor and tumor targeting effects from IVIS imaging*

Taking advantage of the luciferase activity in implanted U87MG cells, antitumor efficacy was also monitored by in vivo bioluminescence imaging after intraperitoneal injection of luciferin and imaging with IVIS. Fig. 11a shows the representative lateral IVIS images of individual mouse from different groups at different time points. In control and laser groups, the BLI increased rapidly with time while in the laser + HA-PEG-MPLs group the BLI apparently remained constant. To further elucidate the treatment efficacy quantitatively, the normalized BLI values (normalized to start of treatment on day 10) of all mice were plotted in Fig. 11b. As evident from the figure, the laser + HA-PEG-MPLs group showed the lowest and the least scattered normalized BLI values among all groups at all time points, endorsing the efficacy and consistency of using HA-PEG-MPLs for combined PTT/PDT.

The tumor-targeting ability of the HA-PEG-MPLs could be also assessed by IVIS with fluorescence imaging from the fluorescent characteristics of encapsulated ICG in HA-PEG-MPLs. As shown in the Fig. 11c, after injection of HA-PEG-MPLs and magnetic guidance for 2 h with a magnet at the tumor site, enhanced accumulation of HA-PEG-MPLs was found at the tumor site, which could be identified in the image with high fluorescence signal [46]. Meanwhile a lower signal showed only in the liver/spleen of mouse could be identified among all organs, which was consistent with a previous report indicating PEG-containing liposomes were mainly accumulated to elevated levels in spleen and liver of mice from the biodistribution study [47]. Therefore, we could confirm that magnetic targeting plus the EPR effects, delivery of HA-PEG-MPLs to solid tumors within a short time (< 2 h) is possible, which upon short-term laser exposure will lead to effective cancer therapy based on combined PTT/PDT as revealed from the xenograft tumor model.

4. Conclusion

Dual targeted HA-PEG-MPLs could be prepared for entrapping CMNPs and ICG and coated with HA-PEG by self-assembly. Photothermal effects after short-term exposure to NIR laser light endorsed HA-PEG-MPLs to be a suitable nano-agent for PTT/PDT as justified from enhanced cytotoxicity toward U87MG cancer cells in vitro. With xenograft mice tumor model, we successfully demonstrated that, due to the targeting effects, HA-PEG-MPLs injected intravenously could be preferentially accumulated at the tumor site in vivo to prevent tumor growth after combination with successive short-term NIR laser irradiation. Taken together, this study successfully provided a simple yet effective alternative modality for cancer nanotherapy based on magnetic carriers.

Acknowledgements

The financial assistance was provided by grants from the Ministry of Science and Technology, Taiwan (MOST106-2221-E-182-056-MY3) and Chang Gung Memorial Hospital (BMRP249, CMRPD2G0081 and CMRPD2G0082). The Center for Advanced Molecular Imaging and Translation at Chang Gung Memorial Hospital, Linkou, and technical assistance provided by Yu-Tin Lai are acknowledged for IVIS experiments.

References

[1] C.P. Leamon, J.A. Reddy, Folate-targeted chemotherapy, Adv. Drug Deliv. Rev. 56 (2004) 1127–1141.
[2] D. Peer, J.M. Karp, S. Hong, O.C. Farokhzad, R. Margalit, R. Langer, Nanocarriers as an emerging platform for cancer therapy, Nat. Nanotechnol. 2 (2007) 751–760.
[3] B. Bahrami, M. Hojjat-Farsangi, H. Mohammadi, E. Anvari, G. Ghalamfarsa, M. Yousefi, Nanoparticles and targeted drug delivery in cancer therapy, Immunol. Lett. 190 (2017) 64–83.
[4] J.H. Fendler, A. Romero, Liposomes as drug carriers, Life Sci. 20 (1977) 1109–1120.
[5] P. Sapra, T.M. Allen, Ligand-targeted liposomal anticancer drugs, Prog. Lipid Res. 42 (2003) 439–462.
[6] M.L. Immordino, F. Dosio, L. Cattel, Stealth liposomes: review of the basic science, rationale, and clinical applications, existing and potential, Int. J. Nanomed. 1 (2006) 297–315.
[7] R. Sen, S. Sahoo, S. Satpathy, Liposomes as drug delivery system: a brief review, Int. J. Drug Devel. Res. 5 (2014) 62–75.
[8] R. Kaur, H. Kaur, G. Joshi, T. Matta, Liposomes: a review in cancer therapy, Res. J. Pharm. Biol. Chem. Sci. 7 (2016) 2273–2290.
[9] M.K. Riaz, M.A. Riaz, X. Zhang, C. Lin, K.H. Wong, X. Chen, Surface functionalization and targeting strategies of liposomes in solid tumor therapy: a review, Int. J. Mol. Sci. 19 (2018).
[10] U. Chitgupi, Y. Qin, J.F. Lovell, Targeted nanomaterials for phototherapy, Nanotheranostics 1 (2017) 38–58.
[11] E.J. Hong, D.G. Choi, M.S. Shim, Targeted and effective photodynamic therapy for cancer using functionalized nanomaterials, Acta Pharm. Sin. B 6 (2016) 297–307.
[12] P. Agostinis, K. Berg, K.A. Cengel, T.H. Foster, A.W. Girotti, S.O. Gollnick, Photodynamic therapy of cancer: an update, CA Cancer J. Clin. 61 (2011) 250–281.
[13] C. Zeng, W. Shang, X. Liang, X. Liang, Q. Chen, C. Chi, Cancer diagnosis and imaging-guided photothermal therapy using a dual-modality nanoparticle, ACS Appl. Mater. Interfaces 8 (2016) 29232–29241.
[14] C. Niu, Y. Xu, S. An, M. Zhang, Y. Hu, L. Wang, Near-infrared induced phase-shifted ICG/Fe_3O_4 loaded PLGA nanoparticles for photothermal tumor ablation, Sci. Rep. 7 (2017) 5490.
[15] V. Shanmugam, S. Selvakumar, C.S. Yeh, Near-infrared light-responsive nanomaterials in cancer therapeutics, Chem. Soc. Rev. 43 (2014) 6254–6287.
[16] R. Mendes, P. Pedrosa, J.C. Lima, A.R. Fernandes, P.V. Baptista, Photothermal enhancement of chemotherapy in breast cancer by visible irradiation of gold nanoparticles, Sci. Rep. 7 (2017) 10872.
[17] X. Mou, Z. Ali, S. Li, N. He, Applications of magnetic nanoparticles in targeted drug delivery system, J. Nanosci. Nanotechnol. 15 (2015) 54–62.
[18] P. Pradhan, R. Banerjee, D. Bahadur, C. Koch, O. Mykhaylyk, C. Plank, Targeted magnetic liposomes loaded with doxorubicin, Methods Mol. Biol. 605 (2010) 279–293.
[19] M. Chu, Y. Shao, J. Peng, X. Dai, H. Li, Q. Wu, Near-infrared laser light mediated cancer therapy by photothermal effect of Fe_3O_4 magnetic nanoparticles, Biomaterials 34 (2013) 4078–4088.
[20] X. Guo, W. Li, L. Luo, Z. Wang, Q. Li, F. Kong, External magnetic field-enhanced chemo-photothermal combination tumor therapy via iron oxide nanoparticles, ACS Appl. Mater. Interfaces 9 (2017) 16581–16593.
[21] S. Klein, A. Sommer, L.V.R. Distel, J.-L. Hazemann, W. Kröner, W. Neuhuber, Superparamagnetic iron oxide nanoparticles as novel x-ray enhancer for low-dose radiation therapy, J. Phys. Chem. B 118 (2014) 6159–6166.
[22] X. Yang, A. Iyer, A. Singh, L. Milane, E. Choy, F.J. Hornicek, X. Yang, A.K. Iyer, A. Singh, L. Milane, E. Choy, F.J. Hornicek, Cluster of differentiation 44 targeted hyaluronic acid based nanoparticles for mdr1 sirna delivery to overcome drug resistance in ovarian cancer, Pharm. Res. 32 (2015) 2097–2109.
[23] B.-P. Jiang, L. Zhang, Y. Zhu, X.-C. Shen, S.-C. Ji, X.-Y. Tan, Water-soluble hyaluronic acid-hybridized polyaniline nanoparticles for effectively targeted photothermal therapy, J. Mater. Chem. B 3 (2015) 3767–3776.
[24] H.-L. Hsu, J.-P. Chen, Preparation of thermosensitive magnetic liposome encapsulated recombinant tissue plasminogen activator for targeted thrombolysis, J. Magn. Magn. Mater. 427 (2017) 188–194.
[25] K. Moriyama, T. Ooya, N. Yui, Hyaluronic acid grafted with poly(ethylene glycol) as a novel peptide formulation, J. Control. Release 59 (1999) 77–86.
[26] S. Khadke, P. Stone, A. Rozhin, J. Kroonen, Y. Perrie, Point of use production of liposomal solubilised products, Int. J. Pharm. 537 (2018) 1–8.
[27] D. Frascione, C. Diwoky, G. Almer, P. Opriessnig, C. Vonach, K. Gradauer, Ultrasmall superparamagnetic iron oxide (USPIO)-based liposomes as magnetic resonance imaging probes, Int. J. Nanomed. 7 (2012) 2349–2359.
[28] H.-J. Yoon, H.-S. Lee, J.-Y. Lim, J.-H. Park, Liposomal indocyanine green for enhanced photothermal therapy, ACS Appl. Mater. Interfaces 9 (2017) 5683–5691.
[29] Y. Ma, S. Tong, G. Bao, C. Gao, Z. Dai, Indocyanine green loaded SPIO nanoparticles with phospholipid-PEG coating for dual-modal imaging and photothermal therapy, Biomaterials 34 (2013) 7706–7714.
[30] S. Uthaman, A.P. Mathew, H.J. Park, B.-I. Lee, H.-S. Kim, K.M. Huh, IR 780-loaded hyaluronic acid micelles for enhanced tumor-targeted photothermal therapy, Carbohydr. Polym. 181 (2018) 1–9.
[31] Y.J. Lu, P.Y. Lin, P.H. Huang, C.Y. Kuo, K.T. Shalumon, M.Y. Chen, J.P. Chen,

Magnetic graphene oxide for dual targeted delivery of doxorubicin and photothermal therapy, Nanomaterials 8 (2018) 193.
[32] O. Szentirmai, C.H. Baker, N. Lin, S. Szucs, M. Takahashi, S. Kiryu, Noninvasive bioluminescence imaging of luciferase expressing intracranial U87 xenografts: correlation with magnetic resonance imaging determined tumor volume and longitudinal use in assessing tumor growth and antiangiogenic treatment effect, Neurosurgery 58 (2006) 365–372.
[33] S. Jeon, C.Y. Yoo, S.N. Park, Improved stability and skin permeability of sodium hyaluronate-chitosan multilayered liposomes by layer-by-layer electrostatic deposition for quercetin delivery, Colloids Surf. B 129 (2015) 7–14.
[34] A.L. Klibanov, K. Maruyama, V.P. Torchilin, L. Huang, Amphipathic polyethyleneglycols effectively prolong the circulation time of liposomes, FEBS Lett. 268 (1990) 235–237.
[35] H. Maeda, Tumor-selective delivery of macromolecular drugs via the EPR effect: background and future prospects, Bioconjug. Chem. 21 (2010) 797–802.
[36] D. Singh, R.K. Gautam, R. Kumar, B.K. Shukla, V. Shankar, V. Krishna, Citric acid coated magnetic nanoparticles: synthesis, characterization and application in removal of Cd(II) ions from aqueous solution, J. Water Process Eng. 4 (2014) 233–241.
[37] N.S. Baharin, N. Muhamad Sarih, S. Mohamad, Novel functionalized polythiophene-coated Fe_3O_4 nanoparticles for magnetic solid-phase extraction of phthalates, Polymers 8 (2016) 117.
[38] R. Perrotta, M. Prieto, S. Alonso, N. Chiaramoni, DSPC liposomes improve transport of L-cysteine and reduce metabolic activity, Brit. Biotechnol. J. 12 (2016) 1–11.
[39] M.L. Briuglia, C. Rotella, A. McFarlane, D.A. Lamprou, Influence of cholesterol on liposome stability and on in vitro drug release, Drug Deliv. Transl. Res. 5 (2015) 231–242.
[40] K.-H. Chang, H.-T. Liao, J.-P. Chen, Preparation and characterization of gelatin/hyaluronic acid cryogels for adipose tissue engineering: in vitro and in vivo studies, Acta Biomater. 9 (2013) 9012–9026.
[41] S. Ghosh, A.Z. Badruddoza, K. Hidajat, Uddin M. Shahab, Adsorptive removal of emerging contaminants from water using superparamagnetic Fe_3O_4 nanoparticles bearing aminated β-cyclodextrin, J. Environ. Chem. Eng. 1 (2013) 122–130.
[42] I.S. Smolkova, N.E. Kazantseva, V. Babayan, P. Smolka, H. Parmar, J. Vilcakova, Alternating magnetic field energy absorption in the dispersion of iron oxide nanoparticles in a viscous medium, J. Magn. Magn. Mater. 374 (2015) 508–515.
[43] S. Shen, S. Wang, R. Zheng, X. Zhu, X. Jiang, D. Fu, Magnetic nanoparticle clusters for photothermal therapy with near-infrared irradiation, Biomaterials 39 (2015) 67–74.
[44] A. Jordan, R. Scholz, P. Wust, H. Fähling, F. Roland, Magnetic fluid hyperthermia (MFH): cancer treatment with AC magnetic field induced excitation of biocompatible superparamagnetic nanoparticles, J. Magn. Magn. Mater. 201 (1999) 413–419.
[45] L.P. Feeley, A.M. Mulligan, D. Pinnaduwage, S.B. Bull, I.L. Andrulis, Distinguishing luminal breast cancer subtypes by Ki67, progesterone receptor or TP53 status provides prognostic information, Mod. Pathol. 27 (2014) 554–561.
[46] Z. Belhadj, C. Zhan, M. Ying, X. Wei, C. Xie, Z. Yan, W. Lu, Multifunctional targeted liposomal drug delivery for efficient glioblastoma treatment, Oncotarget 8 (2017) 66889–66900.
[47] P. Crosasso, M. Ceruti, P. Brusa, S. Arpicco, F. Dosio, L. Cattel, Preparation, characterization and properties of sterically stabilized paclitaxel-containing liposomes, J. Control. Release 63 (2000) 19–30.